Electronic Supporting Information

Hydrogen-bond-driven synergistic regulation of crystallization and interfacial coupling in 1.85 eV wide-bandgap perovskites for high-performance organic tandem solar cells

Qi Wang[a], Yingying Wang[a], Wei Hui[b], Lin Song[b], Xiaopeng Xu[a], Yihui Wu*[a], and Qiang Peng*[a]

[a] School of Chemical Engineering, State Key Laboratory of Advanced Polymer Materials, Engineering Research Center of Alternative Energy Materials & Devices, Ministry of Education, Sichuan University, Chengdu 610065, P. R. China

[b] Frontiers Science Center for Flexible Electronics (FSCFE), Institute of Flexible Electronics (IFE), Northwestern Polytechnical University, Xi'an 710072, P. R. China

*Corresponding authors.

E-mails: yihuiwu@scu.edu.cn (Y.W.); qiangpeng@scu.edu.cn (Q.P.)

Methods

Materials

All the chemicals were used directly without further purification. Lead iodide (≥99.999%), lead bromide (≥99.999%), formamidinium iodide (FAI, 99.9%), NiO_x nanoparticle (99.999%) and C_{60} (99.5%) were purchased from Advanced Election Technology Co. Ltd. Anisole was purchased from Aladdin. RbI (99.9%), dimethylformamide (DMF), dimethyl sulfoxide (DMSO), chlorobenzene (CB), isopropyl alcohol (IPA) and ethyl alcohol (EtOH, 99.5%) were purchased from Sigma-Aldrich. Cesium iodide (CsI, 99.999%) was purchased from Alfa-Aesar. Bathocuproine (BCP, 99%) were purchased from Xi'an Yuri Solar Co. Ltd. (4-(3,6-dimethyl-9H-carbazole-9-yl)butyl) phosphonic acid (Me-4PACz, >99.0%) and propanedioic acid (PPDA, 99%) were purchased from TCI. Propane-1,3-diammonium iodide ($PDAI_2$, ≥99.5%) was purchased from Xi'an e-Light New Material Co, Ltd. PM6 and BTP-eC9 were purchased from Solarmer Materials Inc. PNDIT-F3N was purchased from Volt-Amp Optoelectronic Tech. Co., Ltd, Dongguan, China.

Device fabrication

All perovskite devices were fabricated on the cleaned and patterned FTO substrates (AGC22-8A, Advanced Election Technology Co. Ltd.). The patterned FTO glass substrates were cleaned with a surfactant solution, then soaked in deionized water, acetone, and ethanol in the ultrasonic bath for 20 min each.

Single-junction Wide bandgap (WBG) perovskite sub-cells: After dried with a nitrogen gun and cleaned with ultraviolet ozone for 15 min, the substrates were spin-coated with a thin layer of NiO_x nanoparticle (5 mg/mL aqueous solution) at 2000 rpm for 30 s, and annealed in ambient air at 150 °C for 10 min, then cooled down naturally and transferred to glove box. After that, Me-4PACz (0.5 mg/mL in EtOH) was deposited on the NiO_x at 3000 rpm for 30 s and annealed at 100 °C for 10 min.

The precursor solution of 1.0 M $Cs_{0.2}FA_{0.8}PbI_{1.5}Br_{1.5}$ was prepared by dissolving 137.5 mg of FAI, 52.0 mg of CsI, 115.2 mg of PbI_2, and 275.2 mg of $PbBr_2$ in 1 mL of mixed solvents of DMF and DMSO (v/v = 4:1), which was stirred for 12 h before use. The perovskite solution was filtered with 0.22 μm PTFE filter. After that, 70 μL of perovskite ink was deposited by spin coating at 1000 rpm for 10 s with a ramp of 800, and 6000 rpm for 40 s with a ramp of 2000, 20 seconds into the second step, 110 μL of anisole was deposited onto the substrate. For the PPDA containing samples, different concentrations of PPDA were dissolved in the anti-solvent (Anisole). The wet film was then annealed at 100 °C for 15 min. After the perovskite film was cooled down to room temperature, 50 μL of 1 mg/mL $PDAI_2$ isopropanol/chlorobenzene (v/v = 2:1) solution was coated on the perovskite at 4500 rpm for 25 s and annealed at 100 ºC for 5 min. Then 20 nm of C_{60} was thermally evaporated. After that, 20 nm of SnO_x was deposited on ALD system at around 100 °C. Finally, 120 nm of Ag were thermally evaporated.

Single-junction organic sub-cells: A 15 nm of MoO_x was thermally evaporated onto FTO. To form the bulk heterojunction (BHJ). PM6, BTP-eC9, $PC_{61}BM$ with a weight ratio of 1:1.2:0.3 were dissolved in chloroform (polymer concentration: 7.5 mg/mL with 0.5 vol % of DIO as an additive) and stirred at 70 °C for 2 h. Then, 25 μL of above solution was directly spin-coated on the MoO_x layer at 2500 rpm for 30 s in the N_2 glove box at room temperature, followed by thermal annealing at 90 °C for 5 min. After cooling, a PNDIT-F3N/methanol (0.5 mg/mL) was spin-coated on the active layer at 3000 rpm for 30 s to form the electron transport layer. Finally, 100 nm of Ag were deposited by thermal evaporation.

Perovskite/organic tandem solar cells: After completing the deposition of the C_{60} layer, substrates were transferred to atomic layer deposition chamber, 20 nm of SnO_x was deposited on ALD system at around 100 °C. After the ALD deposition, 1.0 nm of Au and 15 nm of MoO_x were thermally evaporated on top of the SnO_X, respectively, to form the interfacial

recombination layer for the tandem cells. The organic BHJ and electron layer were then sequentially spin-coated on MoO_x, as mentioned above.

Characterization

The top-view and cross-sectional SEM images were acquired using a Hitachi S4800 field-emission scanning electron microscopy system manufactured by Hitachi High Technologies Corporation. AFM was recorded from Bruker Innova atomic microscopy. X-ray Diffraction (XRD) patterns of the perovskite films were recorded on a Bruker D8 advance instrument equipped with Cu Kα radiation (40 kV, 40 mA). Scanning was performed at a rate of 7°/min in the 2θ range from 5-45° with a step size of 0.02 s. The UV-Visible absorption spectra of the solution and thin films were measured from the absorbance model (without integrating sphere) using PerkinElmer Lambda 950 UV-vis spectrophotometer with a scanning rate of 600 nm/min in the range of 900-200 nm at a step bandwidth of 1 nm. The type of baseline calibration was the 100% transmittance baseline. The in-situ UV-vis absorption spectroscopy was recorded with Puguangweishi equipped deuterium light sources from 300 nm to 1100 nm in absorbance mode. The Grazing-incidence wide-angle X-ray scattering (GIWAXS) measurements were conducted at the BL14B1 beamline of Shanghai Synchrotron Radiation Facility (SSRF). The grazing incidence angle was 0.4°. The depth profile of the perovskite film on the FTO/NiO_x/Me-4PACz substrate was recorded using ToF-SIMS (model ION ToF-SIMS 5). The pulsed primary Bi^+ ion source was operated at 30 keV and 0.5 pA on a 100*100 μm^2 area to bombard the sample surface to produce secondary ions. For negative polarity, the sputtering was performed with a Cs ion beam operated at 1.0 keV and 30 nA on a 300*300 μm^2 area. For positive polarity, the sputtering was performed with a O_2 ion beam operated at 1 keV and 60 nA on a 300*300 μm^2 area. The steady PL spectra and time-resolved PL decay measurements were performed using an FLS980 Series of Fluorescence Spectrometers. For the PL measurement, the excitation source was a monochromatized Xe lamp (peak wavelength at 500 nm with a line width of 2 nm). For TRPL, the excitation source was a

supercontinuum pulsed laser sources (YSL SC-PRO) with an excitation wavelength at 514 nm and a repetition rate of 0.1 MHz. Monochromatic external quantum efficiency (EQE) spectra were recorded as functions of wavelength with a monochromatic incident light of 1 x 10^{16} photons cm^{-2} in alternating current mode with a bias voltage of 0 V (QE-R3011). The light intensity of the solar simulator was calibrated by a standard silicon solar cell provided by PV Measurements. A Fourier transform infrared spectroscopy (FT-IR, Thermo Fisher Nicolet Is5) was used to collect the FT-IR spectral data for the samples without and with SA-derivative. Urbach energy (E_U) was detected by HS-EQE (ENLITECH PECT-600) and obtained by fitting the tail of the band. The liquid state ^1H nuclear magnetic resonance (NMR) measurements were recorded on JNM-ECZ400S/L1 spectrometer (TMS as an internal standard ($\delta = 0$)). UPS and XPS spectra were recorded by a Thermo-Fisher ESCALAB Xi+ system. For XPS measurement, radiation was produced by a monochromatic 75 W Al Kα excitation centered at 1486.7 eV. For UPS measurement, He I ultraviolet radiation source of 21.22 eV was used. KPFM measurements were performed on a BRUKER ICON atomic force microscope under a Peak-Force KPFM mode, and the scan rate was 0.5 Hz during the testing process. The samples were scanned in at least three random locations to ensure reliable results. The EQE of electroluminescence (EQE_{EL}) spectra of the PSCs were detected by ENLITECH REPS-V_{OC} under dark conditions. I-V curves were performed at a test range of 0-1.5 V with a step length of 0.02, EL was measured at an applied voltage of 1.2 V, and then I-V and EL were fitted to obtain EQE_{EL}. A LuQY Pro radiative efficiency meter (Model no. LP20-32) was used to perform QFLS measurements. The QFLS values were derived from fitting the high-energy slope of the photoluminescence peak to generalized Planck's law under the assumption that absorptance equals 1 within this energy range. These calculations were automatically performed by the integrated measurement software, which provided direct values of QFLS. The current-voltage characteristics were measured by Keithley 2400 source and the solar simulator with standard AM 1.5G (100 mW cm^{-2}, SAN EI: Japan) under ambient

conditions. The light intensity was calibrated by a Newport-calibrated standard silicon solar cell. The *J-V* curves were measured by forward (-0.1 V to 1.5 V forward bias) or reverse (1.5 V to -0.1 V) scans with a voltage step of 20 mV and a delay time of 100 ms for each point. The active area of a PSC is 0.12 cm^2. The *J-V* curves for all devices were obtained by masking the cell with a metal mask of 0.09 cm^2 in area. The devices for long-term stability measurement were stored in a N_2-filled glovebox. After various periods of time, the *J-V* measurements were performed. The dynamic MPP tracking was carried out in a home-made N_2-filled box under 1 sun continuous illumination (white light LED array) with temperature of ~45 °C (Multi-Channels Solar Cells Stability Test System, Wuhan 91PVKSolar Technology Co. Ltd, China). The MPPT was automatically recalculated every 2 h by tracking the *J-V* curve.

Supplementary Notes

Note S1. Surface free energy

The surface free energy of solids (γ_s) can be modeled according to the assumption that the total surface energy of solids is contributed from polarity and dispersity ($\gamma_s = \gamma_s^p + \gamma_s^d$).[1-3] Basically, the liquid droplet on flat surface following Young's equation:

$$\gamma_{sv} - \gamma_{sl} = \gamma_{lv}\cos\theta$$

Where, γ_{sv}, γ_{sl} and γ_{lv} refer to interfacial tensions at solid-vapor, solid-liquid and liquid-vapor interfaces, respectively. θ is the contact angle of a liquid on a solid surface.

By combining Good's equation:

$$\gamma_{sl} = \gamma_s + \gamma_l - 2(\gamma_s^d\gamma_l^d)^{1/2} - 2(\gamma_s^p\gamma_l^p)^{1/2}$$

The Owens-Wendt equation is as follows:

$$\frac{\gamma_l(1+\cos\theta)}{2(\gamma_l^d)^{1/2}} = (\gamma_s^p)^{1/2}\frac{(\gamma_l^p)^{1/2}}{(\gamma_l^d)^{1/2}} + (\gamma_s^d)^{1/2}$$

Therefore, by plotting $(\gamma_l^p)^{1/2}/(\gamma_l^d)^{1/2}$ versus left part of above equation, the surface free energy of solid γ_s can be calculated.

The above Owens-Wendt model is based on a smooth and homogeneous surface. Furthermore, according to Wenzel Theory, the roughness can be specified by correcting θ with the roughness factor (r):

$$\cos\theta_W = r\cos\theta_Y$$

$$r = \frac{A^{actual}}{A^{projected}}$$

Where, θ_W is the predicted Wenzel contact angle, θ_Y is the Young contact angle, A^{actual} is the solidliquid actual surface area, $A^{projected}$ is the projected area.

Note S2. PL and TRPL measurement

The steady PL spectra and time-resolved PL decay measurements were performed using an FLS980 Series of Fluorescence Spectrometers. For the PL measurement, the excitation source was a monochromatized Xe lamp (peak wavelength at 500 nm with a line width of 2 nm). For TRPL, the excitation source was a supercontinuum pulsed laser sources (YSL SC-PRO) with an excitation wavelength at 514 nm and a repetition rate of 0.1 MHz. The TRPL decay curves were fitted using a bi-exponential function and the fitted data were summarized in Table S2.

$$f(t) = A_1 exp^{\left(-\frac{t}{\tau_1}\right)} + A_2 exp^{\left(-\frac{t}{\tau_2}\right)} + B$$

Where, $\tau_1$represent the fast decay process related to the bimolecular recombination, and $\tau_2$is the slow decay process associated with the trap-assisted recombination process of charge-carrier.[4] B is a constant for the baseline offset. A_1 and A_2 are constants, representing the contributions of the fast and slow components, respectively. The average PL decay lifetime was calculated using following equation:

$$\tau_{ave} = \frac{\sum A_i \tau_i^2}{\sum A_i \tau_i}$$

Note S3. The electron density in the conduction band near the surface of perovskite films

The electron density (n) was calculated by the following equation:

$$n = N_C exp^{\frac{E_C - E_F}{-k_B T}}$$

E_C is the energy levels at the bottom of the conduction band and E_F is the Fermi level; k_B is the Boltzmann constant and T is the absolute temperature, $k_B T$ of 0.0259 eV was used for calculation at 300K. N_C denotes the densities of the conduction band states, which was calculated to be 1.2×10^{19} cm^{-3} for $FAPbI_3$.[5]

Note S4. Calculation of the quasi-Fermi level splitting (QFLS) based on the PL quantum yield (PLQY)

A LuQY Pro radiative efficiency meter (Model no. LP20-32) was used to perform QFLS measurements. These calculations were automatically performed by the integrated measurement software, which provided direct values of QFLS. The direct relation between QFLS and PLQY as the following equation:[6]

$$QFLS = QFLS_{rad} + k_B T \ln(PLQY) = k_B T \ln(PLQY \frac{J_G}{J_{0,rad}})$$

Where, QFLS is the difference between the electron and hole quasi-Fermi levels in the perovskite layer, $k_B T$ of 0.0259 eV was used for calculation at 300 K. J_G is the generation current density under illumination, in this case, approximated to the short-circuit current density J_{SC} of devices. $J_{0,rad}$ is the dark radiative recombination saturation current density.

Note S5. SCLC measurement

The electron-only devices were assembled for the SCLC measurement. The dark I-V curves of the electron-only and hole-only devices can be divided into three parts: Ohmic region, trap-filling limited region with a sharp increase in current and the trap-free Child's region.[7] The trap density, n_t, can be determined using following equation:

$$V_{TFL} = \frac{en_t L^2}{2\varepsilon\varepsilon_0}$$

Where, V_{TFL} is the trap-filled limit voltage, n_t is the trap density, L is the thickness of perovskite film, ε is the relative dielectric constant of the perovskite,[8] and ε_0 is the vacuum permittivity.[9]

Note S6. EQE of EL

The EL spectra of both devices were recorded by a light emitting diode PL quantum-yield measurement system equipped with Enlitech REPS-V_{OC} Source Measurement Unit. The voltage deficit ($V_{loss}^{non-rad}$) related to the non-radiative recombination was calculated using the following equation:[10-11]

$$V_{loss}^{non-rad} = -\frac{k_B T}{q} \ln(EQE_{EL})$$

Where, k_B is the Boltzmann constant, T is absolute temperature, q is the elementary charge, EQE_{EL} is the EQE value of the device working as LED under the injection current equal to that of the J_{SC} of the solar cell.

Supplementary Figures

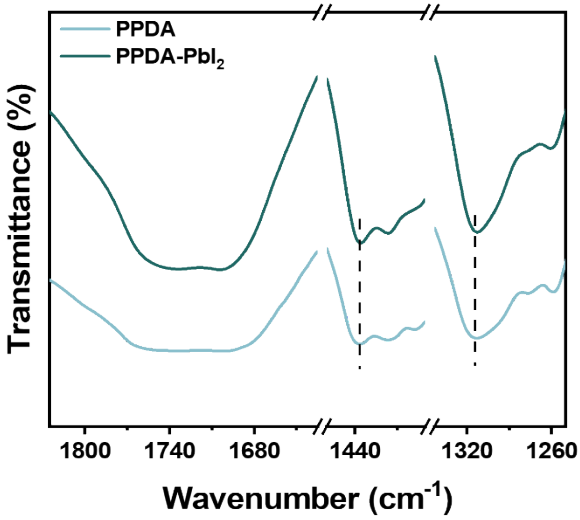

Figure S1. FT-IR spectra of PPDA and PPDAI-PbI_2 films.

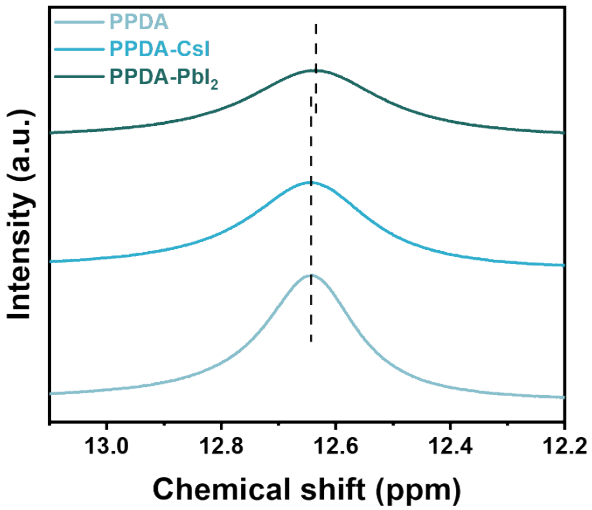

Figure S2. Liquid-state ^{1}H nuclear magnetic resonance (^{1}H-NMR) spectra of PPDA, PPDA-CsI and PPDA-PbI_2.

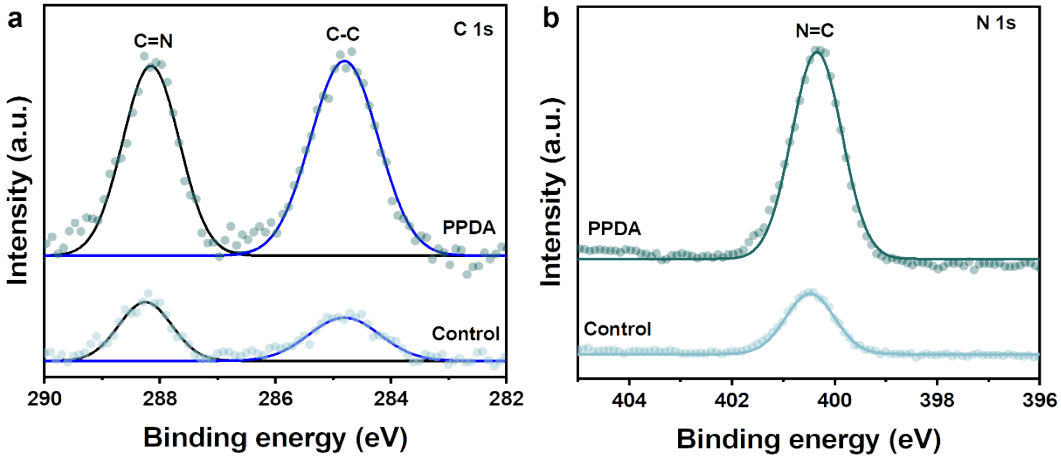

Figure S3. High resolution XPS spectra of (a) C 1s and (b) N 1s for the control and PPDA treated perovskite films.

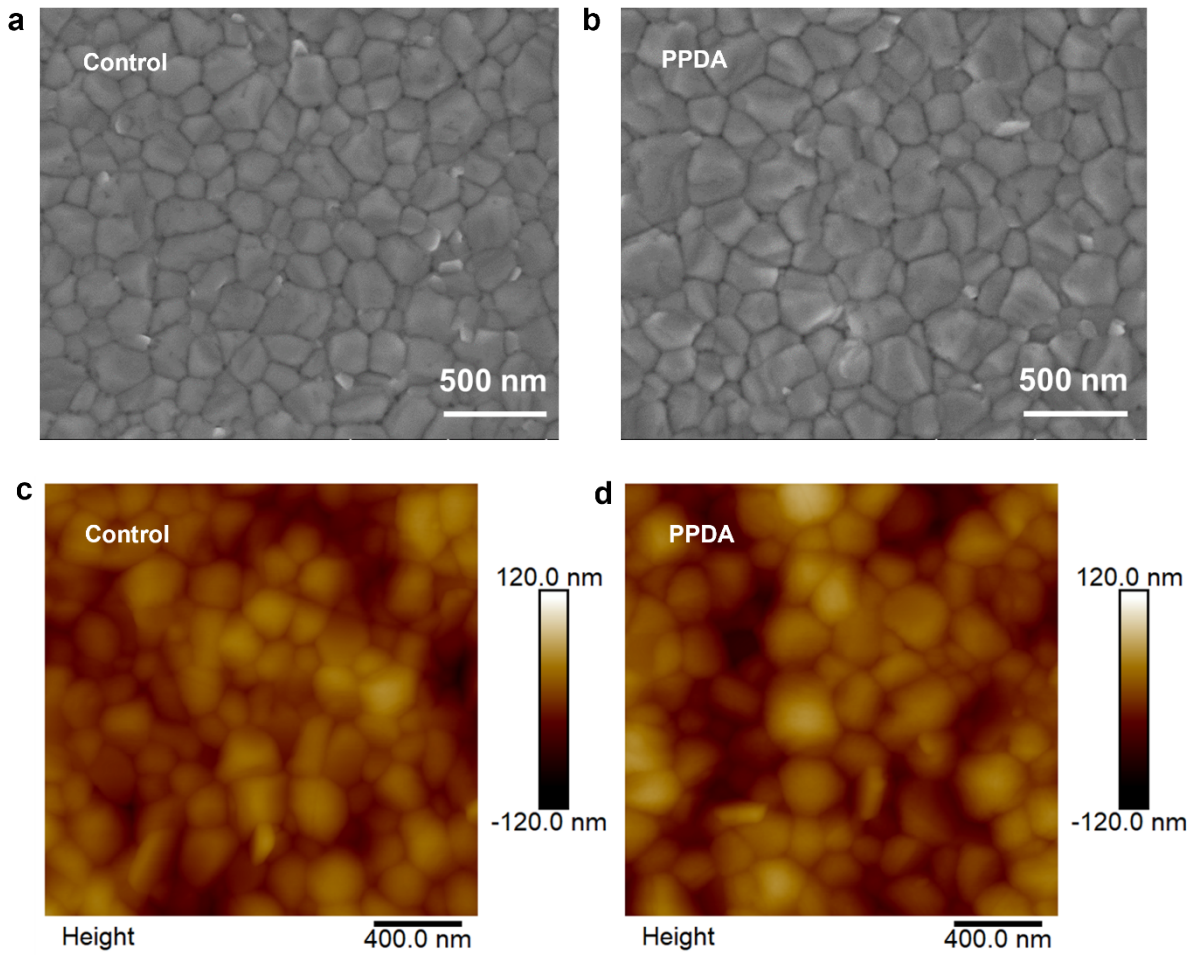

Figure S4. Top-viewed SEM images of (a) the control and (b) PPDA-treated perovskite films. AFM images of (c) the control and (d) PPDA-treated perovskite films.

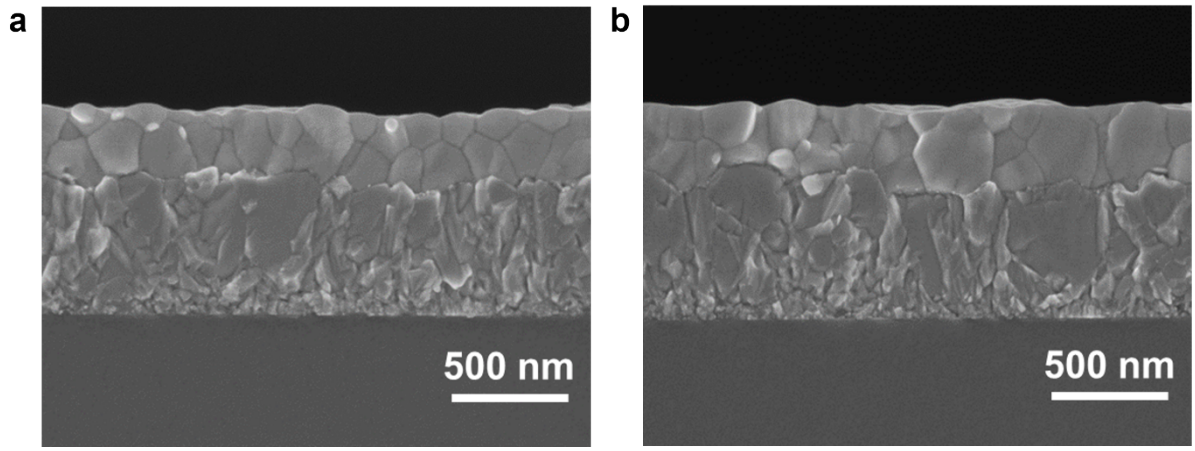

Figure S5. The cross-sectional SEM images of (a) the control and (b) PPDA-treated perovskite films.

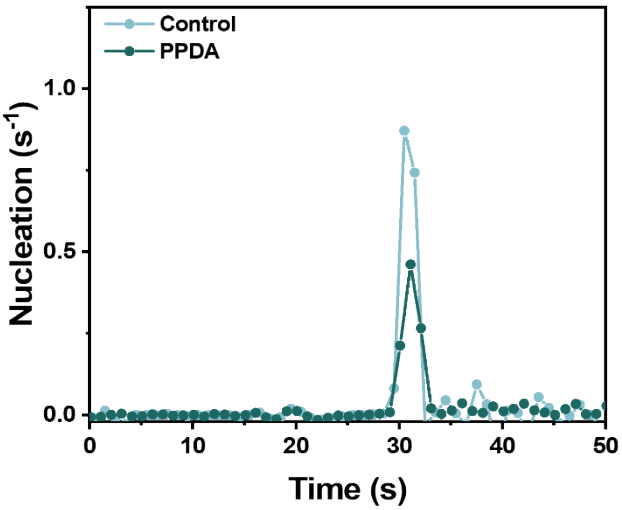

Figure S6. The calculation of nucleation rates for the control and PPDA-treated sample using first derivatives corresponded to in situ UV-vis spectra.

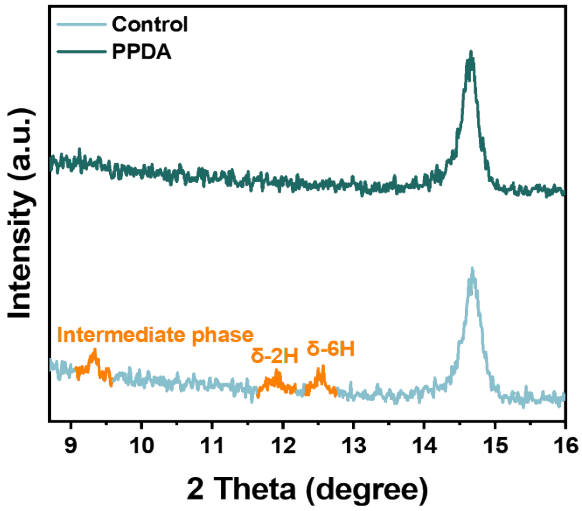

Figure S7. XPD patterns of the control and PPDA treated perovskite films.

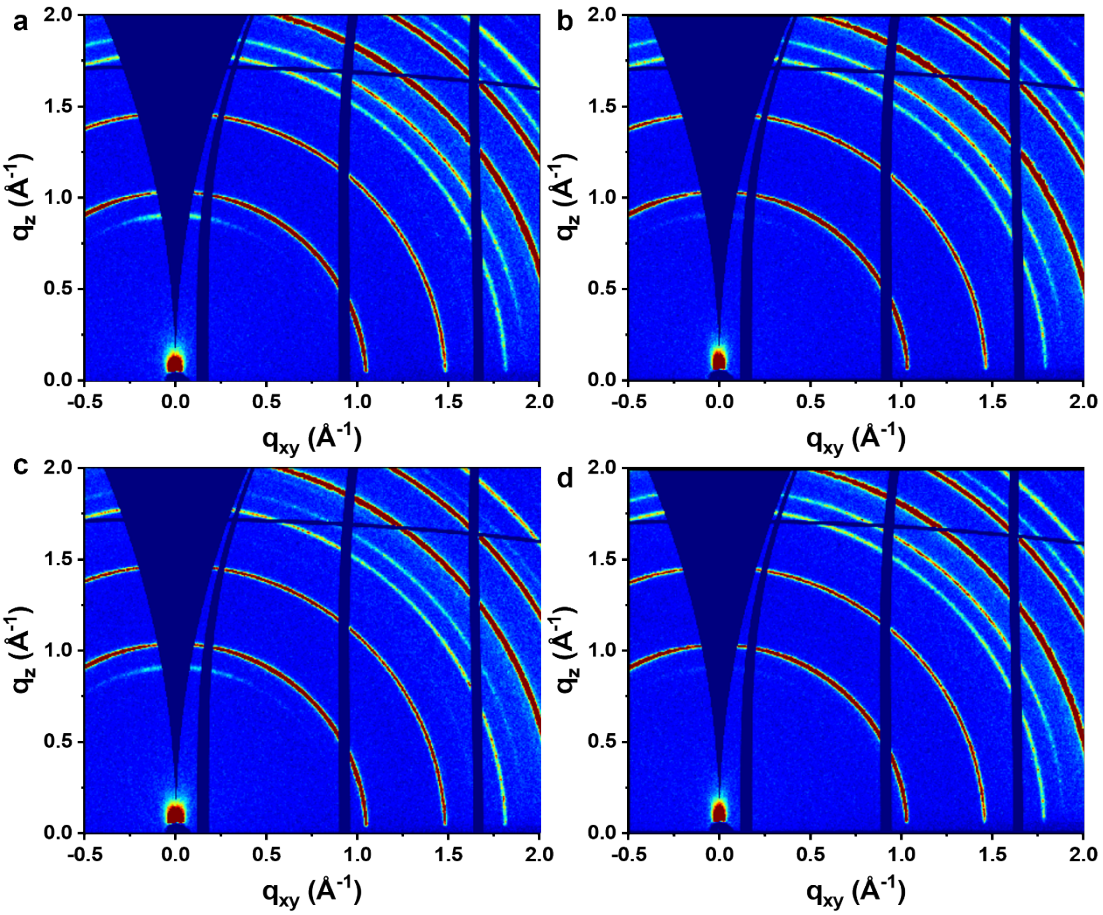

Figure S8. GIWAXS patterns of (a) the control, (b) PPDA, (c) $PDAI_2$, (d) P-$PDAI_2$ treated perovskite films (incident angle = 0.4°).

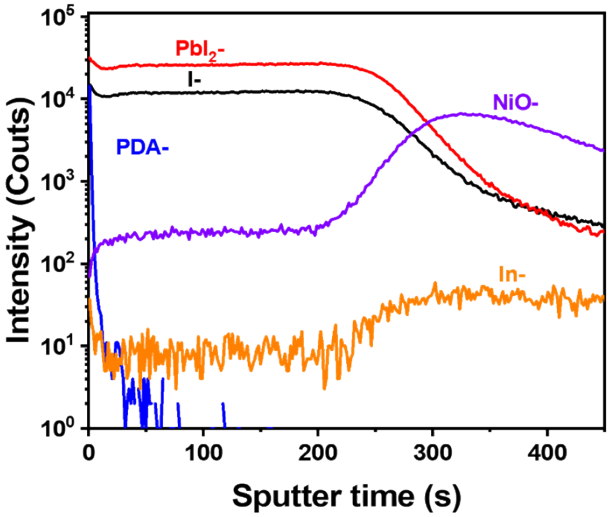

Figure S9. ToF-SIMS depth profiles of the control films treated with $PDAI_2$.

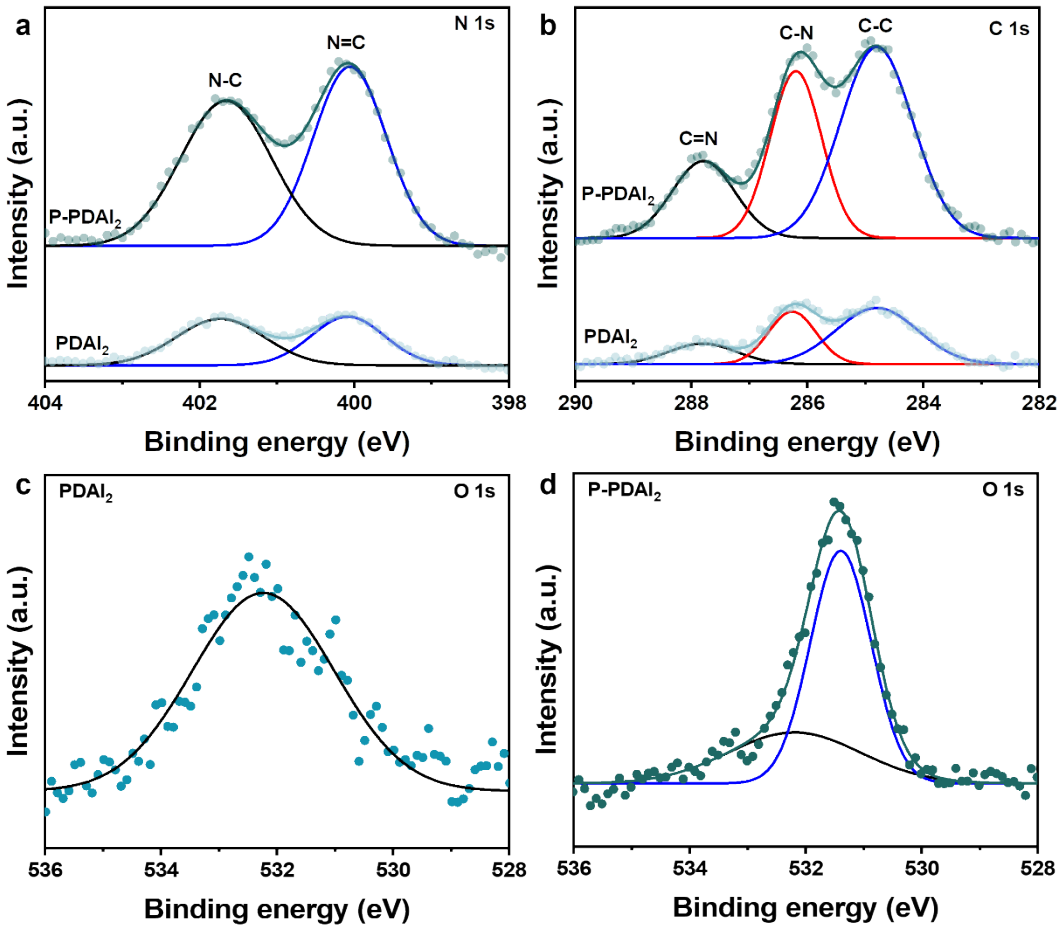

Figure S10. High resolution XPS spectra of (a) N 1s (b) C 1s (c) and (d) O 1s for the control and PPDA perovskite films with and without $PDAI_2$ treatment.

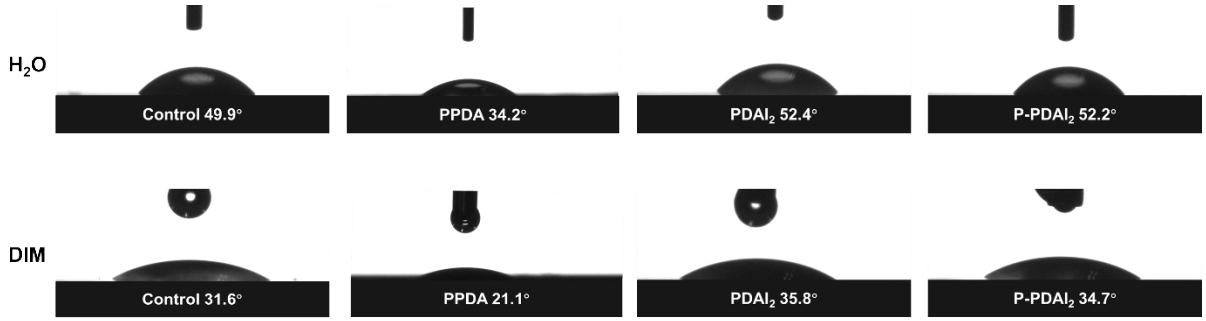

Figure S11. The contact angle (CA) of water and diiodomethane based on perovskite films without and with PPDA and $PDAI_2$ treatment.

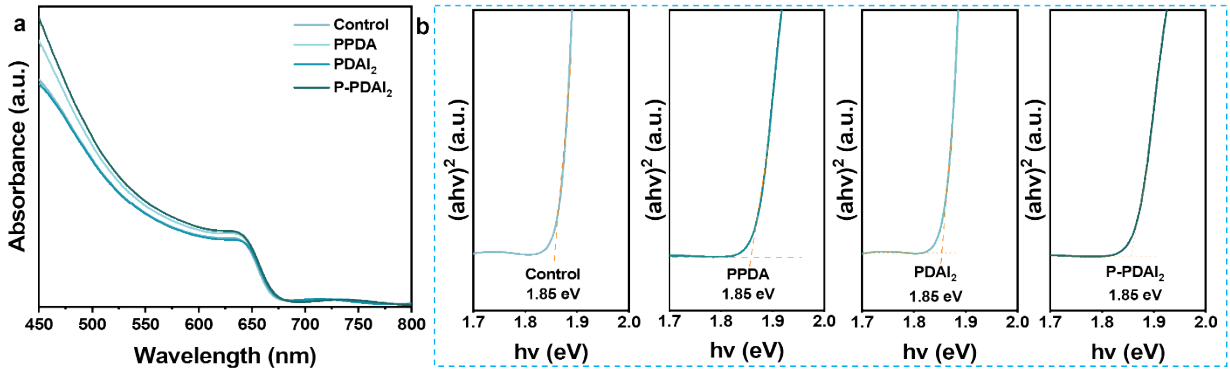

Figure S12. (a) The UV-Vis spectra of the control, PPDA, $PDAI_2$, and P-$PDAI_2$ perovskite films. (b) Tauc plots of the control, PPDA, $PDAI_2$, P-$PDAI_2$ perovskite films from UV-Vis absorption spectra, respectively.

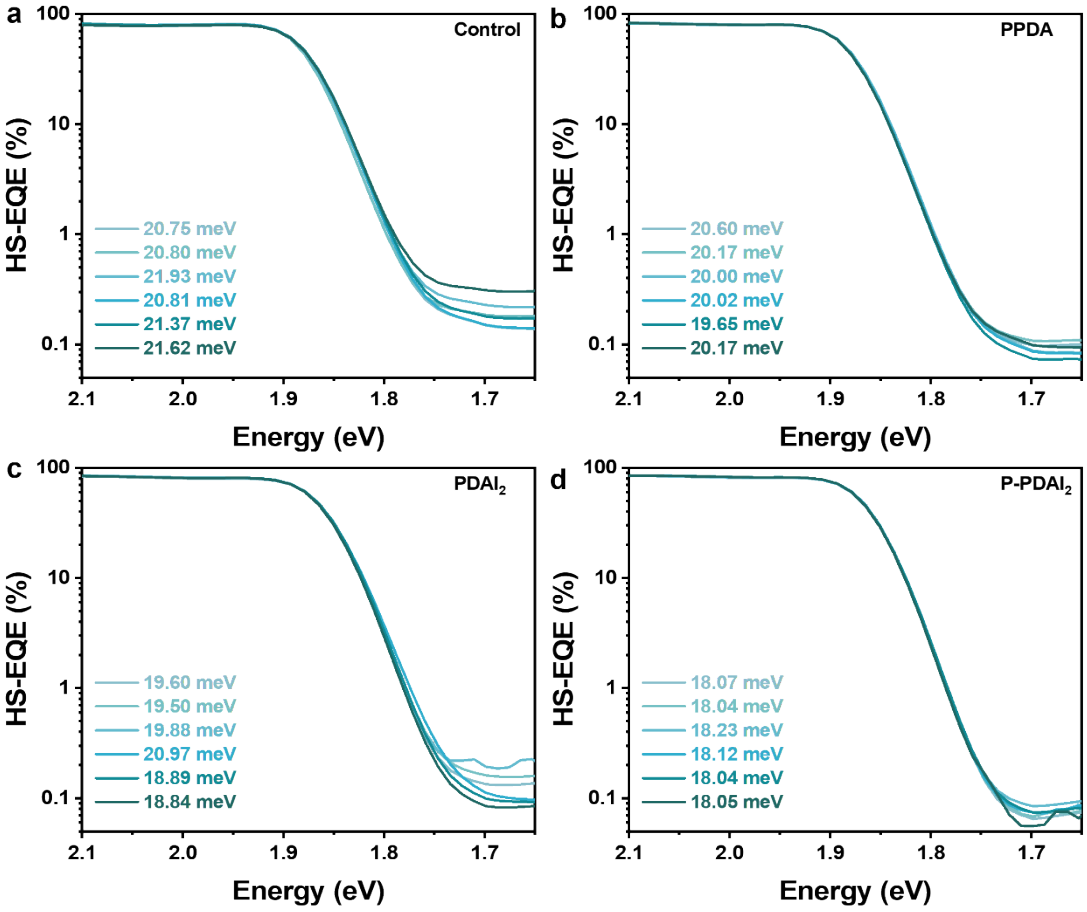

Figure S13. Urbach energy (E_U) curves of (a) the control, (b) PPDA, (c) $PDAI_2$, and (d) P-$PDAI_2$ treated devices.

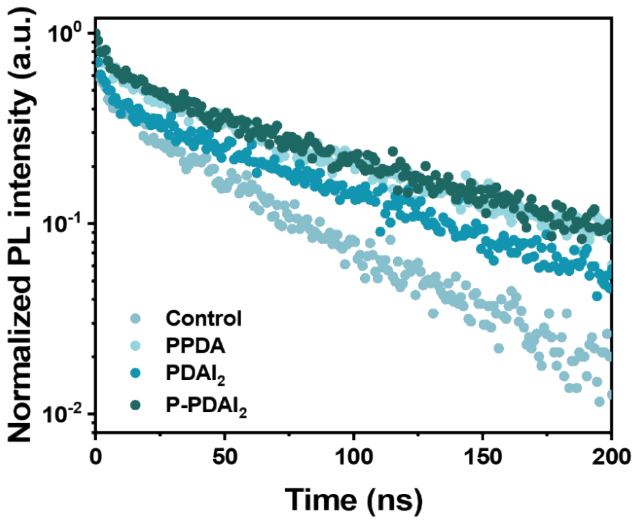

Figure S14. TRPL spectra of the control, PPDA, $PDAI_2$ and P-$PDAI_2$ perovskite films.

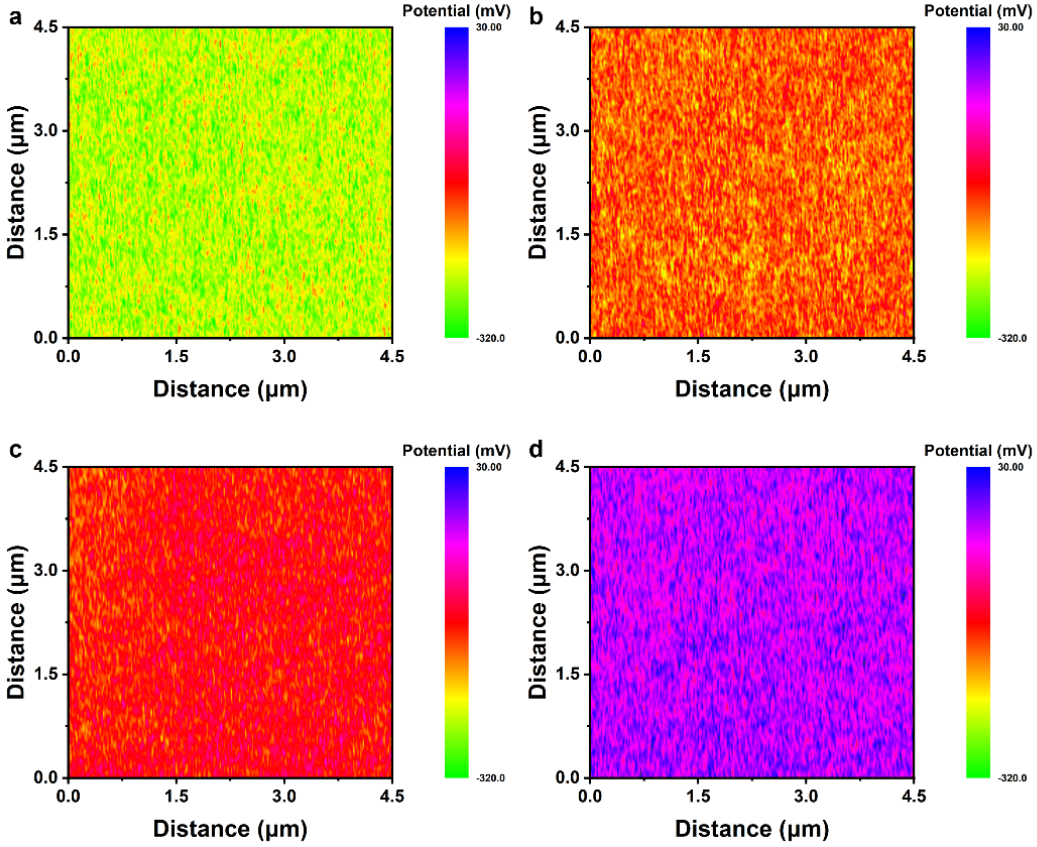

Figure S15. KPFM mapping of (a) the control, (b) PPDA (c) $PDAI_2$, and (d) P-$PDAI_2$ treated perovskite films.

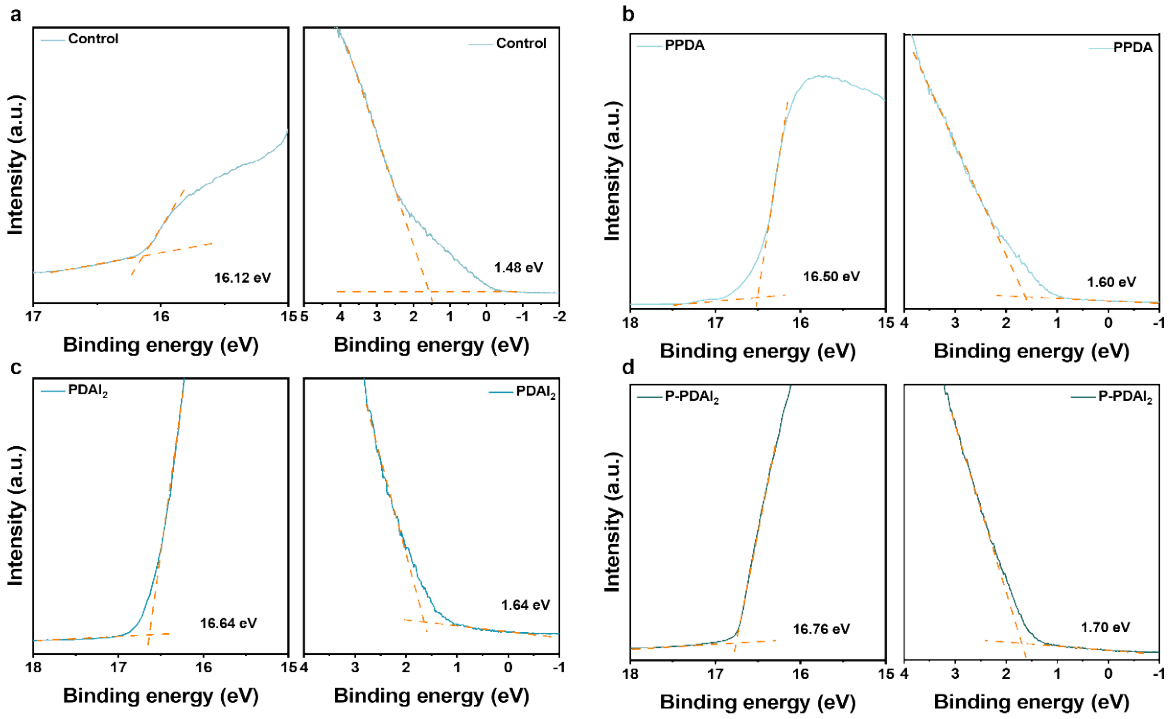

Figure S16. UPS spectra of (a) the control, (b) PPDA, (c) $PDAI_2$, and (d) P-$PDAI_2$ treated perovskite films.

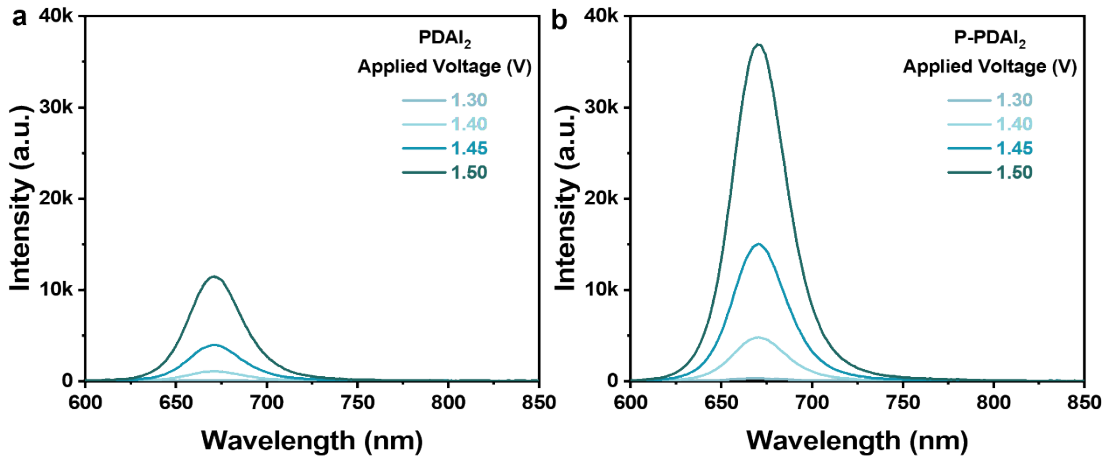

Figure S17. EL emission spectra of (a) $PDAI_2$ and (b) P-$PDAI_2$ treated devices with various applied voltages.

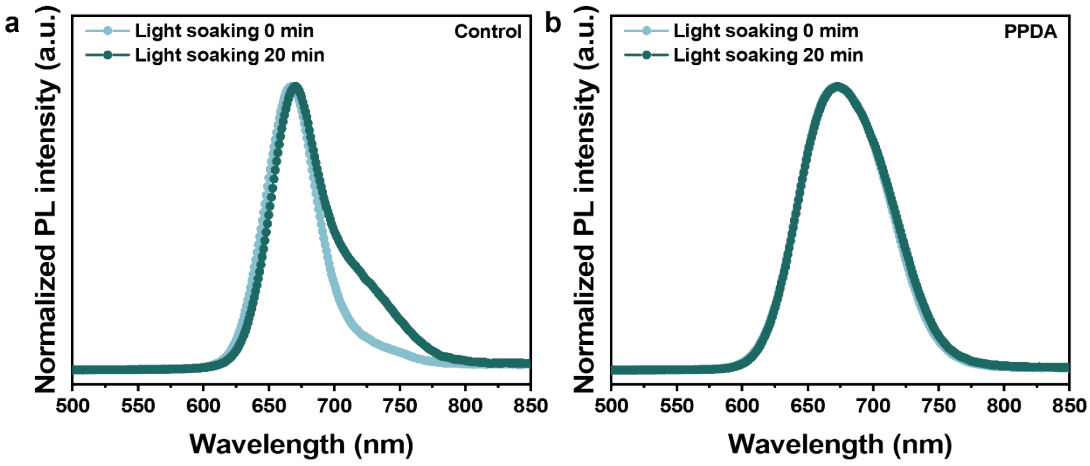

Figure S18. Steady-state PL spectra (a) the control and (b) PPDA treated films on glass substrate.

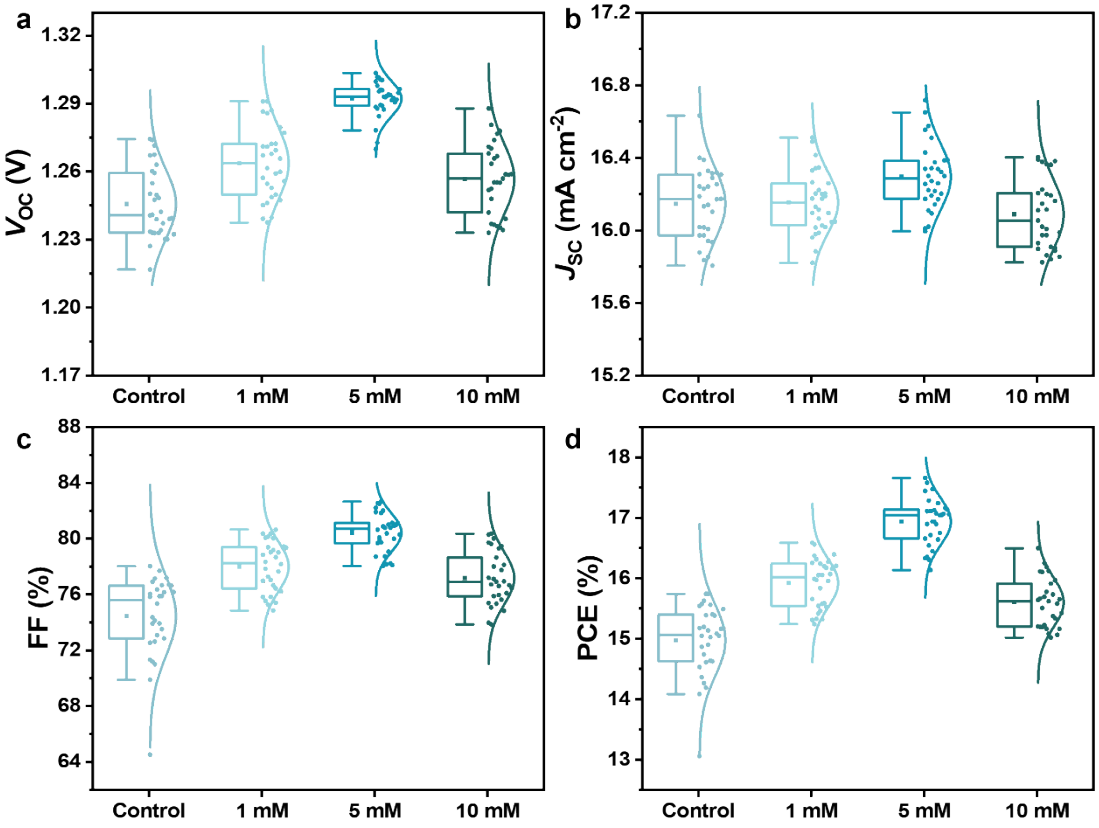

Figure S19. Statistics of the PV parameters for 30 individual devices based on different concentration of PPDA treatment.

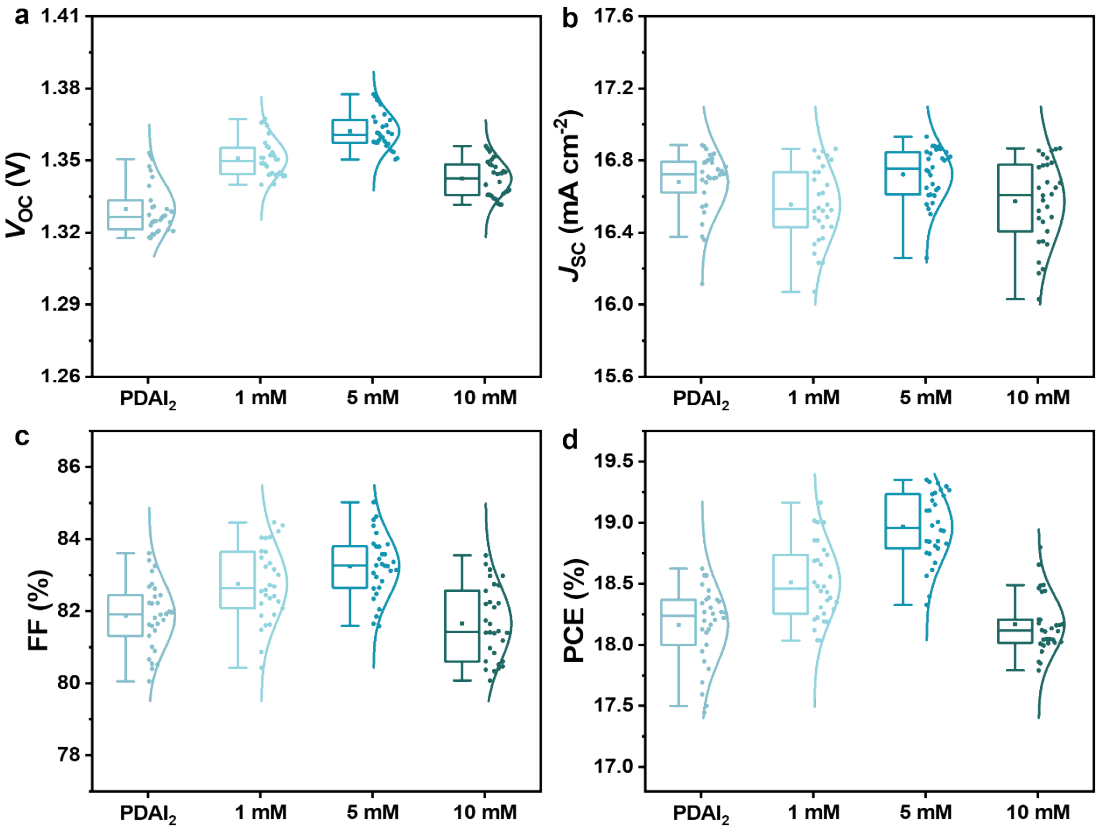

Figure S20. Statistics of the PV parameters for 30 individual devices based on different concentration of PPDA films treated with $PDAI_2$.

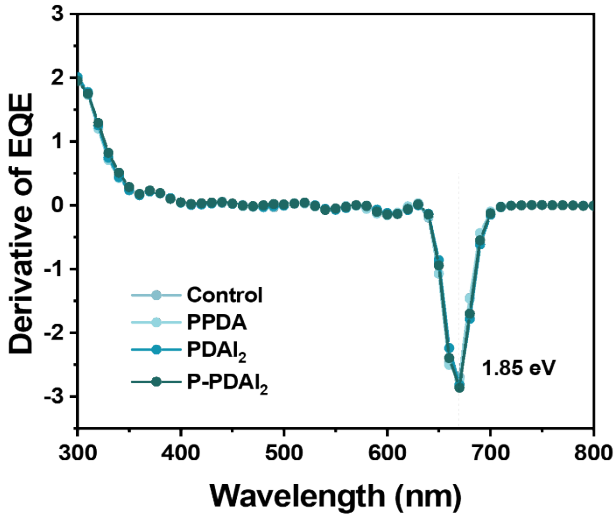

Figure S21. 1st derivative of the EQE spectra for all devices.

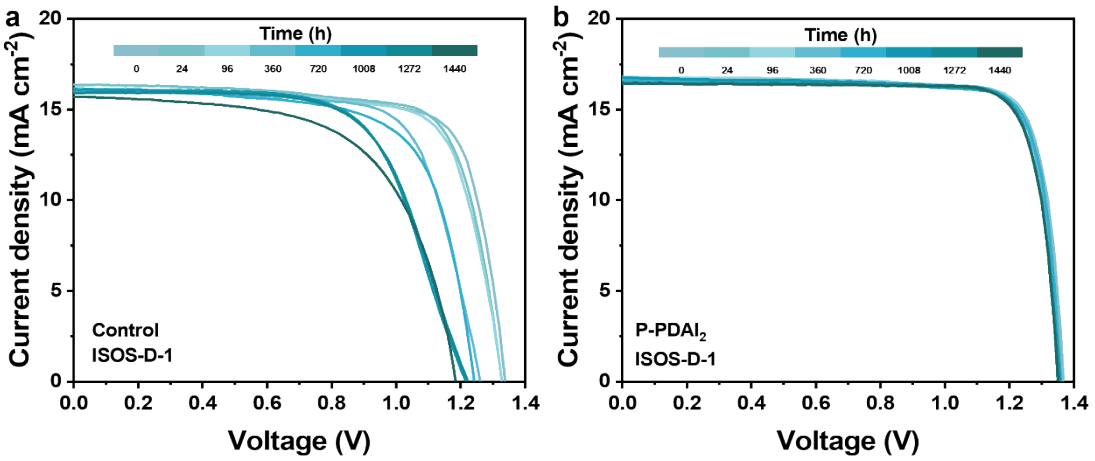

Figure S22. *J-V* curves of (a) the control and (b) P-PDAI$_2$ based devices stored stored in a N_2 filled glovebox at room temperature.

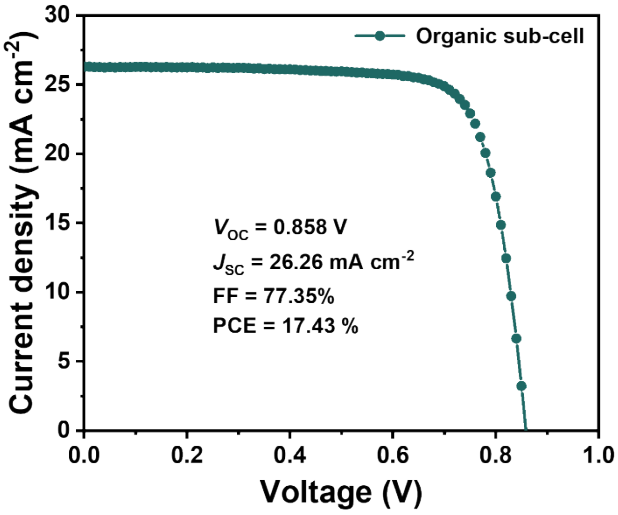

Figure S23. *J-V* curve of single junction organic solar cells.

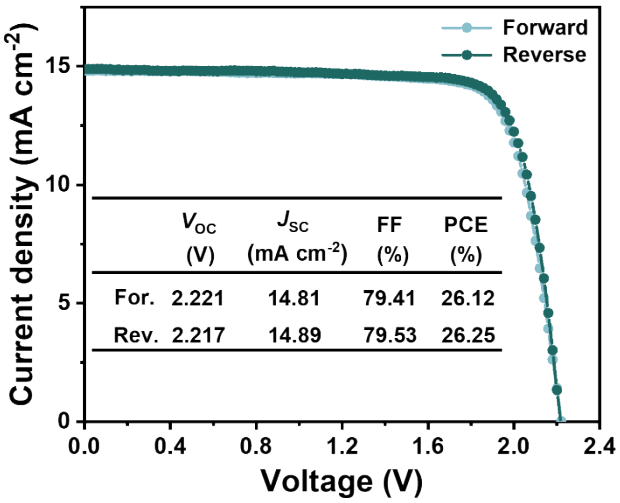

Figure S24. *J-V* curves of POTSCs from reverse and forward scans.

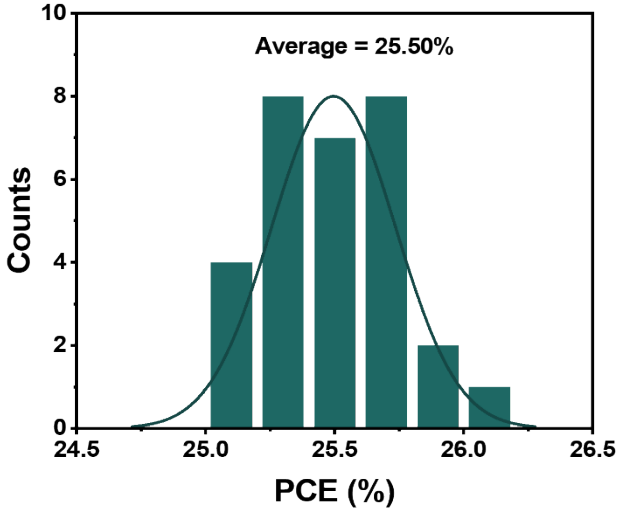

Figure S25. Statistical PCE data of the POTSCs.

Supplementary Tables

Table S1. The calculated results of surface free energy (γ_s). The projected area and actual surface area of substrates are extracted from AFM images.

Substrate	Projected area (μm^2)	Surface area (μm^2)	r	γ_s^p (mJ/m^2)	γ_s^d (mJ/m^2)	γ_s (mJ/m^2)
Control	4.00	4.23	1.058	17.15	45.90	63.05
PPDA	4.00	4.28	1.070	24.52	50.71	75.23
$PDAI_2$	4.00	4.14	1.035	16.24	42.97	59.21
P-$PDAI_2$	4.00	4.12	1.030	16.09	43.32	59.41

Table S2. Parameters of the TRPL spectroscopies based on different samples.

Samples	τ_{ave} (ns)	τ_1 (ns)	τ_2 (ns)	A_1	A_2
Glass/Control perovskite	47.87	1.56	49.49	0.51	0.46
Glass/PPDA-treated perovskite	82.78	4.93	85.87	0.38	0.55
Glass/$PDAI_2$-treated perovskite	78.10	2.04	80.35	0.50	0.43
Glass/P-$PDAI_2$-treated perovskite	83.38	5.57	86.41	0.35	0.58

Table S3. Summary the PV parameters for 30 individual devices based on different concentration of PPDA.

	V_{OC} (V)	J_{SC} (mA cm^{-2})	FF (%)	PCE (%)
0	1.246 ± 0.015	16.14 ± 0.19	74.45 ± 2.89	14.97 ± 0.59
1 mM	1.264 ± 0.015	16.15 ± 0.16	77.99 ± 1.77	15.92 ± 0.40
5 mM	1.292 ± 0.008	16.29 ± 0.18	80.44 ± 1.39	16.93 ± 0.38
10 mM	1.257 ± 0.016	16.08 ± 0.19	77.17 ± 1.89	15.60 ± 0.41

Table S4. Summary the PV parameters for 30 individual devices based on different concentration of PPDA treated with $PDAI_2$.

	V_{OC} (V)	J_{SC} (mA cm^{-2})	FF (%)	PCE (%)
0	1.330 ± 0.011	16.68 ± 0.17	81.87 ± 0.92	18.16 ± 0.31
1 mM	1.351 ± 0.007	16.56 ± 0.21	82.76 ± 1.04	18.51 ± 0.31
5 mM	1.362 ± 0.006	16.72 ± 0.15	83.25 ± 0.86	18.97 ± 0.28
10 mM	1.343 ± 0.007	16.57 ± 0.23	81.65 ± 0.23	18.16 ± 0.23

Table S5. Summary of champion photovoltaic parameters of WBG devices.

	V_{OC} (V)	J_{SC} (mA cm^{-2})	FF (%)	PCE (%)
Control	1.259	16.31	76.64	15.74
PPDA	1.300	16.43	82.66	17.66
$PDAI_2$	1.353	16.74	82.23	18.62
P-$PDAI_2$	1.378	16.65	84.37	19.35

Table S6. Summary of PV parameters for 1.85 eV WBG PSCs.

Perovskite composition	V_{OC} (V)	J_{SC} (mA cm^{-2})	FF (%)	PCE (%)	Ref
$Cs_{0.17}FA_{0.83}Pb(I_{0.44}Br_{0.56})_3$	1.259	15.9	73.4	14.7	[12]
$Cs_{0.2}FA_{0.8}Pb(I_{0.5}Br_{0.5})_3$	1.34	15.6	81	16.8	[13]
$Cs_{0.2}FA_{0.8}Pb(I_{0.5}Br_{0.5})_3$	1.35	16.78	83.29	18.87	[14]
$CsPb(I_{0.75}Br_{0.25})_3$	1.334	16.98	81.61	18.49	[15]
$Cs_{0.1}FA_{0.8}MA_{0.1}Pb(I_{0.5}Br_{0.5})_3$	1.361	16.21	83.21	18.14	[16]
$Cs_{0.2}FA_{0.8}Pb(I_{0.5}Br_{0.5})_3$	1.326	16.64	82.52	18.21	[17]
$Cs_{0.1}FA_{0.8}MA_{0.1}Pb(I_{0.5}Br_{0.5})_3$	1.361	16.27	83.34	18.45	[18]
$Cs_{0.2}FA_{0.8}Pb(I_{0.5}Br_{0.5})_3$	1.339	16.46	86.39	19.06	[19]

$Cs_{0.25}FA_{0.75}Pb(I_{0.5}Br_{0.5})_3$	1.387	16.06	84.20	18.76	[20]
$Cs_{0.2}FA_{0.8}Pb(I_{0.5}Br_{0.5})_3$	1.320	16.2	83.4	17.6	[21]
$Cs_{0.06}FA_{0.66}MA_{0.28}Pb(I_{0.5}Br_{0.5})_3$	1.357	16.49	84.86	19.00	[22]
$Cs_{0.25}FA_{0.75}Pb(I_{0.5}Br_{0.5})_3$	1.300	15.97	82.98	17.24	[23]
$Cs_{0.2}FA_{0.8}Pb(I_{0.5}Br_{0.5})_3$	1.378	16.64	84.37	19.35	This Work

Table S7. Time evolution of the PV parameters for WBG devices.

Devices	Time (h)	V_{OC} (V)	J_{SC} (mA cm^{-2})	FF (%)	PCE (%)
Control	00	1.277	16.14	74.74	15.41
	24	1.268	16.35	73.77	15.29
	96	1.268	16.14	73.19	14.97
	360	1.259	16.00	71.79	14.46
	720	1.241	16.02	69.15	13.75
	1008	1.215	16.09	64.77	12.67
	1272	1.223	15.91	64.74	12.60
	1440	1.184	15.72	61.35	11.41
P-$PDAI_2$	00	1.368	16.60	82.92	18.83
	24	1.361	16.56	83.45	18.82
	96	1.357	16.79	82.59	18.82
	360	1.357	16.63	82.71	18.66
	720	1.357	16.57	82.80	18.62
	1008	1.356	16.76	81.52	18.85
	1272	1.350	16.44	82.87	18.40
	1440	1.351	16.45	82.75	18.38

Table S8. Summary of photovoltaic parameters of WBG, OSC and POTSC devices.

	V_{OC} (V)	J_{SC} (mA cm^{-2})	FF (%)	PCE (%)
WBG	1.378	16.65	84.37	19.35
OPV	0.858	26.26	77.35	17.43
POTSC	2.217	14.89	79.53	26.25

References

1 D. Li, A. W. Neumann, *J. Colloid Interface Sci.* **1992**, 148, 190.

2 A. Kozbial, Z. Li, C. Conaway, R. McGinley, S. Dhingra, V. Vahdat, F. Zhou, B. D'Urso, H. Liu, L. Li, *Langmuir* **2014**, 30, 8598.

3 R. N. Wenzel, *Industrial & Engineering Chemistry* **1936**, 28, 988.

4 Q. Cao, T. Wang, X. Pu, X. He, M. Xiao, H. Chen, L. Zhuang, Q. Wei, H.-L. Loi, P.

Guo, B. Kang, G. Feng, J. Zhuang, G. Feng, X. Li, F. Yan, *Adv. Mater.* **2024**, 36, 2311970.

5 Y. Zhou, G. Long, *J. Phys. Chem. C* **2017**, 121, 1455.

6 M. Stolterfoht, P. Caprioglio, C. M. Wolff, J. A. Márquez, J. Nordmann, S. Zhang, D. Rothhardt, U. Hörmann, Y. Amir, A. Redinger, L. Kegelmann, F. Zu, S. Albrecht, N. Koch, T. Kirchartz, M. Saliba, T. Unold, D. Neher, *Energy Environ. Sci.* **2019**, 12, 2778.

7 L. Liu, Z. Ying, X. Li, H. Du, M. Zhang, J. Wu, Y. Sun, H. Ma, Z. He, Y. Yu, X. Guo, J. Sun, Y. Zeng, X. Yang, J. Ye, *Adv. Energy Mater.* **2025**, 15, 2405675.

8 Q. Han, S. H. Bae, P. Sun, Y. T. Hsieh, Y. M. Yang, Y. S. Rim, H. Zhao, Q. Chen, W. Shi, G. Li, Y. Yang, *Adv. Mater.* **2016**, 28, 2253.

9 C. Zhu, X. Niu, Y. Fu, N. Li, C. Hu, Y. Chen, X. He, G. Na, P. Liu, H. Zai, Y. Ge, Y. Lu, X. Ke, Y. Bai, S. Yang, P. Chen, Y. Li, M. Sui, L. Zhang, H. Zhou, Q. Chen, *Nat. Commun.* **2019**, 10, 815.

10 W. Peng, K. Mao, F. Cai, H. Meng, Z. Zhu, T. Li, S. Yuan, Z. Xu, X. Feng, J. Xu, M. D. McGehee, J. Xu, *Science* **2023**, 379, 683.

11 W. Tress, N. Marinova, O. Inganäs, M. K. Nazeeruddin, S. M. Zakeeruddin, M. Graetzel, *Adv. Energy Mater.* **2015**, 5, 1400812.

12 S. Gharibzadeh, I. M. Hossain, P. Fassl, B. A. Nejand, T. Abzieher, M. Schultes, E. Ahlswede, P. Jackson, M. Powalla, S. Schäfer, M. Rienäcker, T. Wietler, R. Peibst, U. Lemmer, B. S. Richards, U. W. Paetzold, *Adv. Funct. Mater.* **2020**, 30, 1909919.

13 K. O. Brinkmann, T. Becker, F. Zimmermann, C. Kreusel, T. Gahlmann, M. Theisen, T. Haeger, S. Olthof, C. Tückmantel, M. Günster, T. Maschwitz, F. Göbelsmann, C. Koch, D. Hertel, P. Caprioglio, F. Peña-Camargo, L. Perdigón-Toro, A. Al-Ashouri, L. Merten, A. Hinderhofer, L. Gomell, S. Zhang, F. Schreiber, S. Albrecht, K. Meerholz, D. Neher, M. Stolterfoht, T. Riedl, *Nature* **2022**, 604, 280.

14 X. Wang, D. Zhang, B. Liu, X. Wu, X. Jiang, S. Zhang, Y. Wang, D. Gao, L. Wang, H. Wang, Z. Huang, X. Xie, T. Chen, Z. Xiao, Q. He, S. Xiao, Z. Zhu, S. Yang, *Adv. Mater.* **2023**, 35, 2305946.

15 H. Xiao, C. Zuo, L. Zhang, W. Zhang, F. Hao, C. Yi, F. Liu, H. Jin, L. Ding, *Nano Energy* **2023**, 106, 108061.

16 Y. An, N. Zhang, Z. Zeng, Y. Cai, W. Jiang, F. Qi, L. Ke, F. R. Lin, S.-W. Tsang, T. Shi, A. K. Y. Jen, H.-L. Yip, *Adv. Mater.* **2024**, 36, 2306568.

17 X. Wu, D. Zhang, B. Liu, Y. Wang, X. Wang, Q. Liu, D. Gao, N. Wang, B. Li, L. Wang, Z. Yu, X. Li, S. Xiao, N. Li, M. Stolterfoht, Y. H. Lin, S. Yang, X. C. Zeng, Z. Zhu, *Adv.*

Mater. **2024**, 36, 2410692.

18 Y. An, N. Zhang, Q. Liu, W. Jiang, G. Du, D. Chen, M. Liu, X. Huang, T. Lei, Q. Qiu, F. R. Lin, X. C. Zeng, A. K. Y. Jen, H.-L. Yip, *Nat. Commun.* **2025**, 16, 2759.

19 W. Peng, Y. Zhang, X. Zhou, J. Wu, D. Wang, G. Qu, J. Zeng, Y. Xu, B. Jiang, P. Zhu, Y. Du, Z. Li, X. Lei, Z. Liu, L. Yan, X. Wang, B. Xu, *Energy Environ. Sci.* **2025**, 18, 874.

20 Z. Song, J. Wang, Y. Bao, J. Zeng, D. Wang, J. He, P. Zhu, B. Jiang, Z. Liu, S. He, Y. Hou, Z. Hu, C. Xie, Y. Chen, Y. Liu, X. Wang, B. Xu, *Energy Environ. Sci.* **2025**, 18, 4883.

21 Y. Wang, B. Liu, D. Zhang, H. Yu, X. Wu, D. Gao, B. Li, C. Zhang, W. Liu, Z. Yu, N. Wang, L. Wang, X. Li, H. Yan, Z. Zhu, *Small* **2025**, 21, e2411031.

22 G. Xie, H. Li, J. Fang, X. Wang, H. Peng, D. Lin, N. Huang, L. Gan, W. Li, R. Jiang, T. Bu, F. Huang, S. He, L. Qiu, *Angew. Chem. Int. Ed.* **2025**, 64, 202501764.

23 X. Sun, F. Wang, G. Yang, X. Ding, J. Lv, Y. Sun, T. Wang, C. Gao, G. Zhang, W. Liu, X. Xu, S. Satapathi, X. Ouyang, A. Ng, L. Ye, M. Yuan, H. Zhang, H. Hu, *Energy Environ. Sci.* **2025**, 18, 2536.